Comparative Analysis of Image and LiDAR-Based Elevation Maps from a UAV Platform for Agriculture Management

Fangning He[a,*], Magdy Elbahnasawy[a], Tamer Shamseldin[a], A. Habib [a]

[a] Digital Photogrammetry Research Group
Lyles School of Civil Engineering
Purdue University, 550 Stadium Mall Dr., West Lafayette, IN 47907, USA
– (he270, melbahn, tshamsel, ahabib)@purdue.edu

KEY WORDS: UAV, 3D Reconstruction, Image, LiDAR, Precision Agriculture.

ABSTRACT:

Low-cost unmanned airborne vehicles (UAVs) have recently emerged as a promising platform for remote-sensing data acquisition to satisfy the needs of various applications. To date, utilization of UAVs, which are equipped with RGB-frame cameras and geo-referenced laser scanners, for precision agriculture and high throughput phenotyping has gained significant attention from researchers in both mapping and plant science fields. Although, several research efforts have been exerted towards both image-based and LiDAR-based 3D reconstruction with UAV platforms, unfortunately, almost no research has been conducted on a quantitative comparison of these approaches for precision agriculture applications. In this paper, we introduce two approaches for image-based and LiDAR-based Digital Surface Models (DSMs) generation using a multi-rotor UAV platform. Then, a comparative analysis is performed on the DSMs that are derived from real dataset acquired over an agriculture field. The experimental results demonstrate the feasibility of the proposed approaches in providing reliable 3D reconstruction for precision agriculture applications.

1. INTRODUCTION

Nowadays, due to the global challenge of ensuring crop yield for food and fuel generation, precision agriculture, which aims at optimizing crop yield while preserving resources, has gained tremendous interest from researchers in plant science as well as other fields (Habib et al., 2017). Among various applications, high throughput phenotyping is an important precision agricultural approach that combines methodologies and protocols to quantify plant growth, structure, and composition at multiple scales over the growing season (Fiorani and Schurr, 2013). Traditional phenotyping is based on destructive and labor/time-consuming approaches that are mainly conducted in a controlled environment with limited coverage such as greenhouses. In order to alleviate these disadvantages, many research efforts have been conducted on remote sensing-based phenotyping, as it is nondestructive and noninvasive while being capable of providing abundant and diversified information (Araus and Cairns, 2014). To date, with the ever-increasing technological developments in Mobile Mapping Systems (MMS), several platforms, such as mobile sensor systems onboard tractors, tethered balloons, and manned aircrafts, have become attractive options (Busemeyer et al., 2013; Deery et al., 2014). However, some financial and technical constraints (e.g., the initial investment, mobilization cost, and the required technical expertise of end users) prevent the widespread adoption of such human-operated systems. Alternatively, unmanned airborne vehicles (UAVs) have recently emerged as a promising platform for remote-sensing data acquisition to satisfy the needs of various applications. Compared to those human-operated mobile mapping systems, advantages of UAV-based platforms include low cost, ease of storage and deployment, ability to fly lower and collect high-resolution data, and filling an important gap between wheel-based and manned airborne platforms (He and Habib, 2016). Among the possible MMS platforms, UAVs are now becoming competitive platforms for remote sensing-based phenotyping (Habib et al., 2016; Honkavaara et al., 2013; Ribera et al., 2016; Zhang and Kovacs, 2012).

From a mapping point of view, current UAV-based 3D mapping can be achieved through either active or passive remote sensing systems. Active sensors, such as laser scanners, directly provide precise and dense point clouds along the mapped objects. Although, several consumer-grade direct geo-referencing units have been introduced to the market, significant initial investment for the acquisition of a high-end GNSS/INS Position and Orientation System (POS) is still required, especially when seeking high level of reconstruction accuracy. Derived point clouds from active sensors usually lack spectral information, which are needed for the derivation of better and more reliable interpretation to the reconstructed objects. On the other hand, passive sensors, which commonly utilize digital line/frame imaging sensors, can be incorporated for 3D reconstruction while providing spectral attributes for the derived elevation information. However, automated identification of conjugate features in overlapping images, which is commonly known as the matching problem, remains to be a challenging task. For agricultural applications, the matching problem is further complicated by repetitive patterns and/or lack of unique texture within the covered area.

Although, several research efforts (He and Habib, 2016; Wallace et al., 2014, 2012) have been exerted towards UAV-based 3D reconstruction using different remote sensing modalities (i.e., active and passive sensors), it is worth noting that almost no research has been conducted on quantitative comparing of these approaches when dealing with a multi-rotor UAV platform (e.g., DJI S1000+) for precision agriculture applications. Therefore, this paper aims at providing a comparative analysis of the derived Digital Surface Models (DSMs) from a UAV platform, which is equipped with a SONY Alpha 7R digital camera and a Velodyne VLP16 laser scanner aided by the Applanix APX-15 UAV GNSS/Inertial OEM unit. To be more specific, this paper will be focusing on the following issues:

1. Automated image-based DSM generation using UAV-based imagery, which is acquired over agriculture field with repetitive patterns and insufficient texture,

2. Automated laser-based DSM generation using a direct geo-referencing process with consumer-grade GNSS/INS unit, and
3. Comparison of image-based and laser-based DSMs.

To address these issues, the utilized system configuration is introduced in the next section. Then, the proposed methodology for image-based and LiDAR-based DSM generation is explained. Afterwards, the experimental results derived from real datasets are discussed. Finally, drawn conclusions and recommendations for future work are presented.

2. SYSTEM CONFIGURATION

In this section, we investigate the specifications of each individual component of the utilized UAV platform, which ensures that the system will be capable of satisfying the needs of precision agriculture applications. To be specific, this system includes a direct geo-referencing (DG) or navigation unit based on an integrated IMU and GNSS receiver board, one active optical imaging unit and one passive imaging unit. All these components are rigidly fixed within the UAV platform as shown in Figure 1.

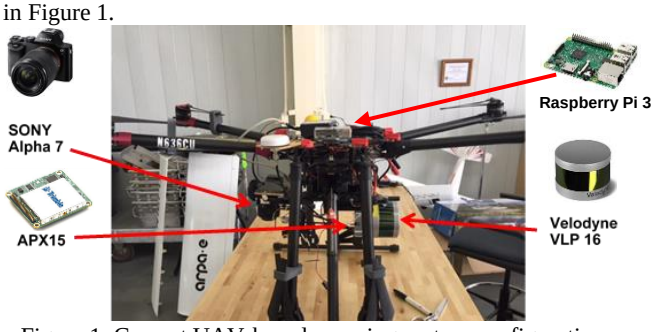

Figure 1. Current UAV-based mapping system configuration

2.1 Platform Selection

For precision agriculture application, we want to maximize the flight duration and minimize the payload. Also, since we will use both LiDAR and cameras on the same system, a multi rotor drone UAV will be more suitable than a fixed-wing UAV. Price wise, the cheaper UAV is, of course, the better.

Considering the DJI S1000+ as the UAV platform, it is designed for professional aerial mapping applications, as well as providing some advantages such as safety, stability and ease of use. It is a vertical take-off and landing UAV that weighs approximately 4.4 Kg without batteries and its maximum takeoff weight is 11 Kg. It can fly for 15 minutes with takeoff payload of 9.5 Kg, which means that this time increases as the weight decreases. The S1000+ will allow to have around 4 to 5 Kg payload of sensors/equipment to be installed on the mapping system (DJI, 2017). The specification of the DJI S1000+ UAV is presented in Table 1.

	Specifications
Weight	4.4 kg
Take-off Weight	6 kg 11 kg
Stator Size	41 x 14 mm
Power Requirements	Lithium-Polymer (LiPo): - Maximum: 4000 W - Hovering: 1500 W at 9.5 kg take-off weight

Table 1. DJI S1000+ UAV Specifications

2.2 Navigation Unit

Generally, the manipulation of the collected optical data requires the geo-referencing of the mapping platform, which means the determination of the position and the orientation of the individual sensors relative to a user-defined coordinate system (Chiang et al., 2012). It is worth noting that the geo-referencing of a mobile LiDAR system has to be established using on an integrated GNSS/INS system, which is known as direct georeferencing (Chiang et al., 2015). On the other hand, the geo-referencing of passive-sensors (i.e., RGB frame camera) can be achieved through either an indirect or direct geo-referencing. The main advantages of direct geo-referencing include reducing or even eliminating the ground control requirement, which is quite useful in mapping remote and inaccessible areas, as well as reducing the cost of the overall mapping process (establishing ground control is the most expensive mapping task next to the deployment of the data acquisition platform). Therefore, the incorporation of GNSS/INS position and orientation system has become the default for the majority of UAV-based mapping platforms. For this research, the Applanix APX-15 UAV is considered due to its low weight, compact size, and precise, robust positioning and orientation information. Regarding the post-processing mode, the unit estimates pitch and roll with 0.025 degree and heading (yaw) with 0.08 degree of accuracy and the position accuracy is 0.02-0.05 meter. The position, roll, pitch, and heading output can be extended up to 100 Hz as illustrated in Table 2 (Applanix, 2017).

	Specifications
Weight	60 grams
Size	67 L x 60 W x 15 H mm (nominal)
Power	8-32 V DC
Position Accuracy (post processing)	0.02 - 0.05 (m)
Velocity Accuracy (post processing)	0.015 (m/sec)
Roll & Pitch Accuracy (post processing)	0.025 (deg)
Heading Accuracy (post processing)	0.080 (deg)
IMU data rate	200 Hz
GNSS data rate	5 Hz

Table 2. APX-15 Specifications

2.3 Active Sensor

In this research, a Velodyne VLP-16 is used for the selected UAV platform. Axes definitions and specifications of the Velodyne VLP 16 are shown in Figure 2 and Table 3, respectively.

Velodyne VLP-16 is a small LiDAR unit, it has 16 lasers beams, which are aligned over the range of +15.00 degrees to -15.00 degrees that provides the vertical field of view (ω), and it delivers a 360-degree horizontal field of view (α). The VLP-16 does not have visible rotating parts. The VLP-16 generates a point cloud of up to 300,000 points per second with a range of 100 meters and typical accuracy of +/- 3 cm at 5-20 Hz (Velodyne LiDAR, 2017).

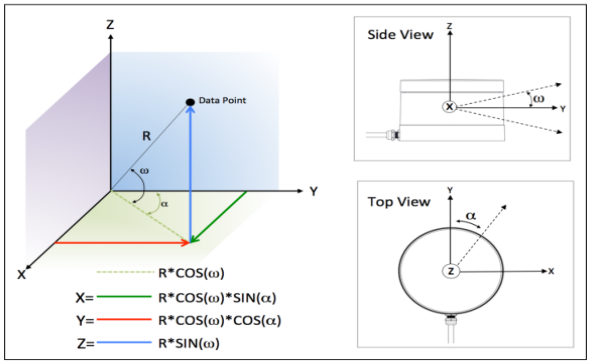

Figure 2. Velodyne VLP16 axes (spherical to XYZ)

	Specifications
Weight	830 grams
Number of channels	16
Horizontal Field of View (FOV)	360°
Vertical Field of View (FOV)	30°
Angular resolution (horizontal/azimuth)	0.1° -0.4°
Rotational speed	5-20 rotations per second (adjustable)
Returns range of	up to 100 meters
Modes of operation	Single and Dual return modes (strongest/last)
3D LiDAR data point generated	Single return mode: ~300,000 points per second Dual return mode : ~600,000 points per second

Table 3: Velodyne VLP16 Specifications

2.4 Passive Sensor

For the camera, there are a variety of selections, either high-end industrial cameras or commercial cameras. For the high-end cameras, they have many wiring controls for both triggering and strobe signals, however, in terms of the price, they are expensive. These controls enable the camera to have an accurate time tagged images and there are no synchronization problems. On the other hand, for the commercial cameras, there are no such controls either for triggering or strobes, which will cause synchronization issues. For the current platform, a commercial camera, Sony alpha 7R, which is 35mm full frame and 36.4 Mega Pixels size, is used to minimize the overall cost of the system. The synchronization issues are addressed through alternative solutions for the triggering and strobe signals. The specifications of the Sony alpha 7R camera are shown in Table 4.

	Specifications
Weight	465 grams
Size	127 x 94 x 48 mm
Sensor	36.3 megapixel
Continuous shooting	4 fps
Flash x-sync	1/160 sec
Approximate Pixel Pitch	4.88 microns
Sensor size:	861.6mm2 (35.90mm x 24.00mm)

Table 3: Sony Alpha 7R Specifications

2.5 Data Storage Media

Unlike the Sony alpha 7R camera, which has a built-in memory card for storing images, VLP16 LiDAR has about 8 megabits/second data rate and it needs an appropriate media for storing the collected data in a given mission. Mini computers are investigated for this purpose but its weight is about 500 gm, which means almost 10% of the UAV payload is used. Alternatively, Raspberry Pi 3 with 1.2 GHz 64-bit quad-core ARMv8 CPU is used with around 50 gm weight. This choice saved around 90% of the weight compared with other selection. Besides, its smaller dimensions make it easier to select its installation spot on the UAV.

3. METHODOLOGY

In this section, the proposed methodology for image-based and LiDAR-based DSM generation is presented. Specifically, the image-based approach is first introduced. Then, the LiDAR-based approach is discussed.

3.1 Image-based DSM generation

As shown in Figure 3, the proposed methodology for image-based DSM generation can be summarized as three steps:

1- The image-based DSM generation starts with the Structure from Motion (SfM) approach, which has been developed by He and Habib (2014), for automated aerial triangulation of the captured image frames. Similar to most SfM-based approaches, the proposed procedure includes three steps. In the first step, the relative orientation parameters (ROPs) relating stereo-images are derived from conjugate point features. In this research, considering the fact that UAV-based imagery acquired for precision agriculture applications usually contain repetitive patterns and/or lack of unique texture within the covered area, two approaches are proposed for reliable estimation of ROPs. Different from the conventional methods, whether it is based on a non-linear (Mikhail et al., 2001) or closed-form solution (Nistér, 2004), the proposed approaches take advantage of prior information regarding the flight trajectory, and is capable of dealing with overlapping images in the presence of high percentage of matching outliers. Interested readers can refer to He and Habib (2016) for more information about the two proposed approaches. Once the ROPs of all possible stereo-pairs are estimated, an incremental approach is adopted for the initial recovery of the image EOPs. Specifically, the incremental approach is initiated by defining a local coordinate frame. Then, all images are sequentially augmented into a final image block. Once the initial approximate EOPs are estimated, a feature tracking procedure, which aims at identifying conjugate point features from multiple overlapping images, is adopted. Finally, a bundle adjustment process, which utilizes the estimated image EOPs as well as the tracked tie points, is conducted to refine the derived image EOPs as well as coordinates of 3D object points.

2- Since the derived image EOPs and the sparse point cloud are only defined in an arbitrary local coordinate system, an absolute orientation process has to be conducted to establish the transformation from the local frame to the mapping coordinate system. In this research, in order to estimate the 3D similarity transformation parameters (i.e., scale factor, three translation parameters, and three rotation angles) relating local and mapping coordinate systems, tie points corresponding to the GCPs are first manually identified. Then, the 3D coordinates of tie points, which are defined in the local coordinate system, are computed through a spatial intersection. Afterwards, the transformation parameters are estimated using the GCPs and their corresponding local coordinates. Finally, the set of estimated parameters are used to transform the derived image EOPs as well as 3D object coordinates from the local coordinate system to the mapping

frame. Now that the 3D similarity transformation has been applied, an indirect geo-referencing process, which utilizes a global bundle adjustment, is conducted to refine the derived geo-referencing parameters. One should note that, in this implemented bundle adjustment process, GCPs are used for datum definition.

3- Given the geo-referenced EOPs, image-based dense point cloud can be generated through dense image matching techniques. Among different approaches, the semi-global matching (SGM) algorithm (Hirschmuller, 2005), which minimizes the image matching costs along several one-dimensional path directions through the image, has recently emerged as a promising technique for image-based dense reconstruction. To date, several research efforts (Gerke, 2009; Hirschmüller and Bucher, 2010) have demonstrated that the SGM is capable of offering a good matching accuracy for various applications. The SGM is originally established on normalized image stereo-pairs, where the stereo images are re-sampled in a way that the epipolar lines are parallel to the x-axis of the image. Although the utilization of such normalized stereo images is sufficient for some computer vision applications, where stereo-cameras are used for data acquisition, it may significantly increase the computational expense for most mapping applications, which mainly deal with sets of overlapping images. In order to overcome this limitation, an object space-based approach is proposed in this research. To be more specific, the proposed approach has several characteristics:

- Rather than generating normalized image stereo-pairs, the proposed approach is performed on a dense voxel established in the object space. Based on such configuration, it is not necessary to derive the matching cost in image space. Instead, the matching cost can be directly formulated on each voxel using all images, which could be more advantageous for mapping applications.
- The semi-global optimization can be conducted in the voxel space with 16 paths, which leads to the direct derivation of image-based dense point cloud.
- The sparse point cloud derived from the bundle adjustment process can be used to facilitate the image-based point cloud generation procedure. Specifically, the utilization of the prior knowledge regarding the reconstructed objects is capable of reducing the search range in the voxel space, which results in improvement of reconstruction accuracy as well as decrease of processing time. Finally, a regular DSM can be generated based on the derived image-based dense point cloud.

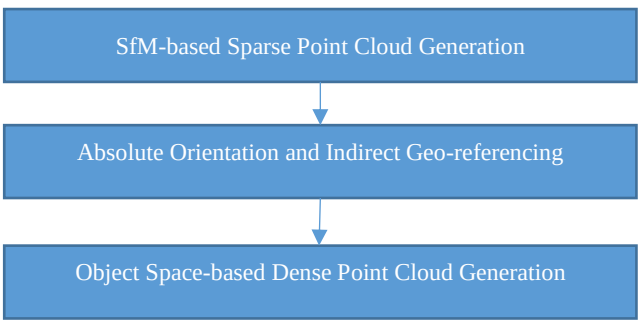

Figure 3. Proposed work flow for image-based DSM generation

3.2 LiDAR-based DSM generation

Improvements of the direct geo-referencing technology led to a positive impact on the adoption of LiDAR systems for the acquisition of dense and accurate surface models for precision agriculture applications. In general, a UAV-based LiDAR system requires two main components: an integrated GNSS/INS to provide position and orient information, and a laser scanner to provide the range/distance from the laser-beam firing point to its footprint. Usually, GNSS and INS are integrated in one GNSS/INS module known as DG unit. With the utilization of DG unit, LiDAR systems can directly provide an accurate DSM with a dense set of irregular points, surpassing the quality of those derived from other techniques, such as manual photogrammetric DSM generation, radar interferometry, and contour interpolation.

For this research, the integrated GNSS/INS (APX-15) unit supplies sequentially precise time pulses, known as pulse-per-second (PPS) signals to LiDAR (VLP16), which is responsible for triggering the active sensor (laser scanner unit) every second. Synchronization to GNSS pulse-per-second (PPS) signals gives the capability of determining the exact firing time of each laser beam, and should be received by the interface box of the active sensor. In addition, the integrated GNSS/INS unit provides a navigation message in NMEA format ($GNRMC message), which includes information regarding position, rotation, and GNSS time (Velodyne LiDAR, 2017). This navigation message is recorded over a dedicated RS-232 serial port and is received by the laser scanner via the interface box in the form of serial data, which should be at 9600 baud rate.

An illustration of the different coordinate systems of a GNSS/INS-assisted mobile LiDAR unit is represented in Figure 4. As shown in the figure, the coordinates of a given point ***I*** relative to the mapping reference frame can be derived through a vector summation process as can be seen in Equation 1.

$$r_I^m = r_b^m(t) + R_b^m(t) r_{lu}^b + R_b^m(t) R_{lu}^b R_{lb}^{lu}(t) r_I^{lb}(t) \qquad (1)$$

In this equation, $r_b^m(t)$ and $R_b^m(t)$ are the position and the orientation of the IMU body frame relative to the mapping reference frame, and they are derived through the GNSS/INS integration process. r_{lu}^b and R_{lu}^b are the lever arm vector and boresight matrix, which relate the LiDAR unit coordinate system and IMU body frame. One should note that both r_{lu}^b and R_{lu}^b are time independent since the IMU and LiDAR units are rigidly fixed onboard the platform. They can be derived through a calibration process. $r_I^{lb}(t)$ is the range between the laser beam firing point and point ***I***. $R_{lb}^{lu}(t)$ defines the rotation between the laser beam and the laser unit coordinate systems. Both $r_I^{lb}(t)$ and $R_{lb}^{lu}(t)$ are obtained from the LiDAR unit measurements.

Given the LiDAR equation, one can conclude that the accuracy of the LiDAR point cloud depends on the quality of the measurements from the individual system components and their spatial relationship as defined by the mounting parameters. Even though the measurements of the individual system components (GNSS, INS and LiDAR) are quite precise, serious errors can result from inaccurate estimation of the mounting parameters. Therefore, precise LiDAR system calibration is necessary to ensure the accuracy of the point cloud generation process. In this research, since the data acquisition is conducted over an agricultural field, almost no suitable features can be utilized for the calibration.

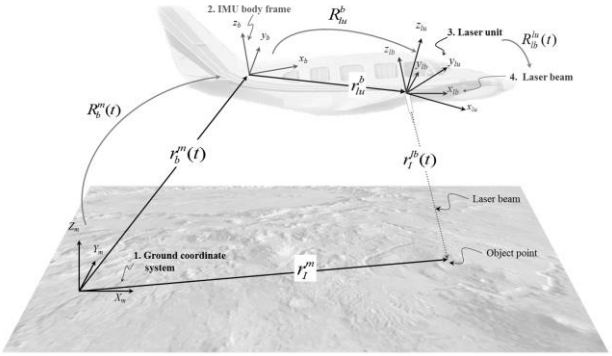

Figure 4. Coordinate Systems and Vector Summation in LiDAR Equation (Habib, 2016)

In order to overcome such challenge, a novel calibration board design, which could be easily deployed and setup within indoor and outdoor environments as well as giving the ability to facilitate the identification of conjugate planar features, is proposed. To be more efficient, the calibration boards are combined with high reflective surfaces (stop signs) with known dimension, which increase the speed of the automation process of target detection. The new calibration boards are shown in Figure 5. In this research, calibration is done at the beginning of the data collection process, keeping the same system configuration and conditions, and at the end of the data collection to ensure the system calibration stability and robustness. The proposed calibration mainly depends on extracting planar features from the new calibration boards with reflective surfaces.

Figure 5. Calibration boards with reflective surface for aerial system

4. EXPERIMENTAL RESULTS

In this section, the comparative analysis is conducted on image-based and LiDAR-based DSMs that are derived from real datasets using the proposed methodology.

4.1 Dataset Description

The test site involved in the experiments covers an agriculture field at Purdue University's Agronomy Center for Research and Education (ACRE) in Wester Lafayette, United States. The main characteristics of the acquired image and laser datasets are described as below.

The **Image Dataset** is comprised of 639 images that are captured from thirteen flight lines with approximate 60% overlap and side lap (See Figure 6 (a) and (b) for sample images). The flying height of the utilized DJI S1000+ UAV is approximate 40 meters and the flying speed is roughly 8 m/s. Moreover, 10 GCPs and 26 check points are established. Both GCPs and check points are surveyed by an RTK GPS with an approximate accuracy of $\pm 2\ cm$. Then, the root-mean-square-error (RMSE) for the check points is evaluated after conducting the bundle adjustment as described in Section 3.1. For this experimental dataset, the RMSE values for the X, Y, and Z coordinates are 0.03 m, 0.03m, and 0.04 m, respectively, which indicates a good accuracy of the image-based 3D reconstruction.

Due to the limited battery endurance, the **LiDAR Dataset** is acquired on the same day in a separate mission with eight flight lines. The flying height of the UAV platform is approximate 45 meters and the flying speed is 5 m/s. A total number of 25 million laser points is acquired over the involved test site (See Figure 6 (c) for a sample area of the reconstructed laser points).

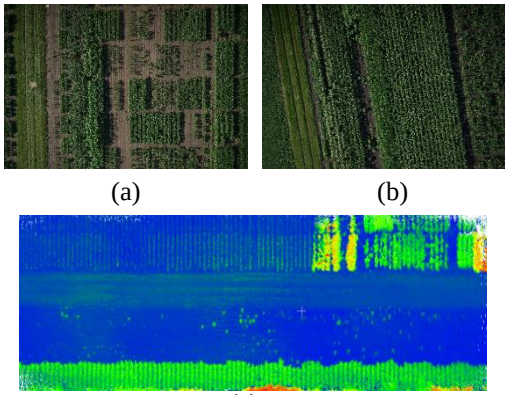

(a) (b)

(c)

Figure 6. (a) and (b) two sample images from the image dataset, and (c) a sample area from the laser dataset (laser points are colorized based on elevation)

4.2 Accuracy Analysis

Now that the image-based and LiDAR-based point clouds are generated, the DSMs are interpolated at four-centimeter Ground Sampling Distance (GSD). For qualitative evaluation of the derived DSMs, six spatially-distributed profiles are generated across the whole field. The width of each profile is 12 centimeters. Figure 7 illustrates the image-based and LiDAR-based profiles. Looking into these profile figures, it is evident that the two DSMs are capable of providing comparable height reconstruction in the selected areas. Moreover, one can also observe that some points from the LiDAR-based DSM are below the image-based DSM. This is mainly because the laser beam can penetrate through the gaps between the leaves while the image-based reconstruction can only define the top of the canopy.

For the quantitative evaluation, both correlation analysis and statistical calculations (e.g., RMSE) are conducted to examine the similarity between the image-based and LiDAR-based heights within the same profiles. The formula for computing the RMSE value is presented in Equation 2.

$$RMSE = \sqrt{\frac{\sum_{i=1}^{n}(Z_{x,y}^{image} - Z_{x,y}^{LiDAR})^2}{n}} \quad (2)$$

Where, $Z_{x,y}^{image}$ and $Z_{x,y}^{LiDAR}$ are the Z values extracted from the same location (x, y) in the image-based and LiDAR-based DSMs. The derived correlation and RMSE values are reported in Table 5. From such results, one can conclude the following:

• The minimum correlation between the image-based and LiDAR-based height estimation is 0.75, which indicates good positive correlations between the DSMs that are derived from the two different approaches.

• Another observation to note is that the derived RMSE values range from 0.36 m to 0.49 m. As it has been explained earlier, this is mainly because the laser beam is able to penetrate through the gaps between the leaves, which results in the points reconstructed underneath the canopy layer.

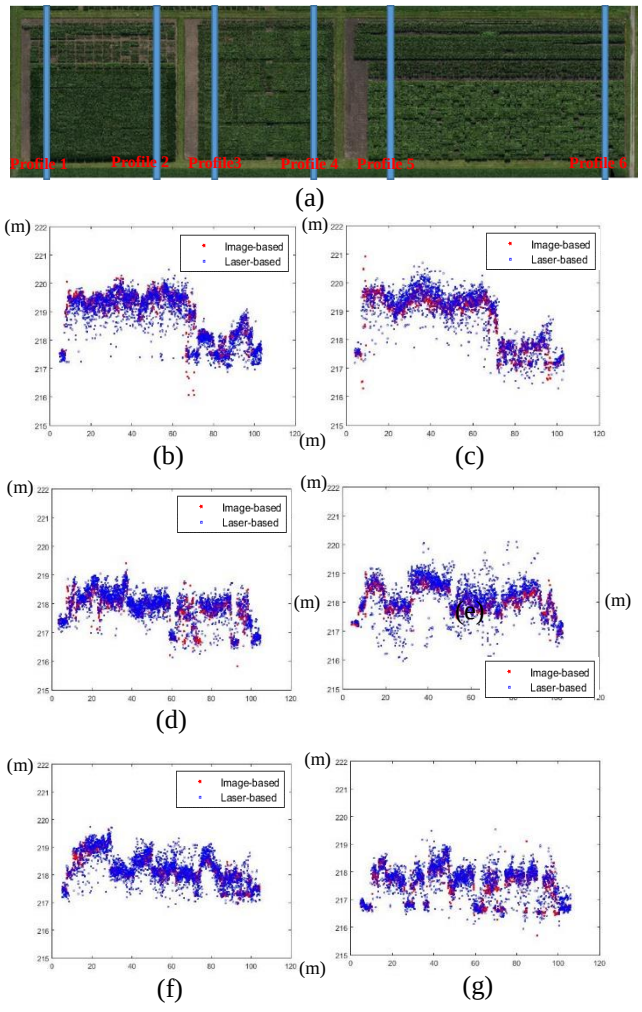

Figure 7. (a) Locations of selected profiles, and (b) to (g) cross section of profiles 1 to 6 (the image-based DSM is shown in red, and the laser-based DSM is visualized in blue).

Profile	Correlation (R)	RMSE (m)
1	0.85	0.49
2	0.84	0.48
3	0.76	0.36
4	0.75	0.37
5	0.76	0.42
6	0.77	0.37
Overall	0.86	0.39

Table 5. Correlation (*R*) and RMSE calculation between the image-based and laser-based DSMs

5. CONCLUSIONS AND RECOMMENDATIONS FOR FUTURE WORK

In this paper, we investigated the performance of both image-based and LiDAR-based 3D reconstruction from a UAV platform for precision agriculture applications. Then, a comparative analysis was performed on the derived image-based and LiDAR-based DSMs. For the experimental test, a DJI S1000+ multi-rotor UAV with a SONY Alpha 7R digital camera and a Velodyne VLP16 laser scanner is utilized. By performing both qualitative and quantitative evaluation, we can draw the conclusion that the proposed image-based and LiDAR-based approaches are capable of providing comparable 3D reconstruction for precision agriculture applications.

It is worth noting that current image-based DSM generation is achieved through an indirect geo-referencing procedure, which is quite inefficient and time-consuming. In order to alleviate such problem, the GPS-assisted triangulation and direct geo-referencing, which utilizes the consumer-grade GNSS/INS unit onboard the UAV platform, will be investigated for the image-based DSM generation. In addition, considering the fact that high throughput phenotyping aims at accurate estimation of important phenotypic traits, such as height, canopy closure and leaf structure, the feasibility of using remote sensing-based (i.e., image-based and LiDAR-based) techniques for plant traits estimation will be studied for future work.

ACKNOWLEDGEMENT

The information, data, or work presented herein was funded in part by the Advanced Research Projects Agency-Energy (ARPA-E), U.S. Department of Energy, under Award Number DE-AR0000593. The views and opinions of authors expressed herein do not necessarily state or reflect those of the United States Government or any agency thereof.

REFERENCES

Applanix, 2017. APX-15 UAV - Applanix [WWW Document]. APX15UAVApplanix.URLhttps://www.applanix.com/downloads/products/specs/APX15_DS_NEW_0408_YW.pdf (accessed 3.9.17).

Araus, J.L., Cairns, J.E., 2014. Field high-throughput phenotyping: the new crop breeding frontier. Trends Plant Sci. 19, 52–61.

Busemeyer, L., Mentrup, D., Möller, K., Wunder, E., Alheit, K., Hahn, V., Maurer, H.P., Reif, J.C., Würschum, T., Müller, J., others, 2013. Breedvision—A multi-sensor platform for non-destructive field-based phenotyping in plant breeding. Sensors 13, 2830–2847.

Chiang, K.-W., Tsai, M.-L., Chu, C.-H., 2012. The Development of an UAV Borne Direct Georeferenced Photogrammetric Platform for Ground Control Point Free Applications. Sensors 12, 9161–9180. doi:10.3390/s120709161.

Chiang, K.-W., Tsai, M.-L., Naser, E.-S., Habib, A., Chu, C.-H., 2015. New Calibration Method Using Low Cost MEM IMUs to Verify the Performance of UAV-Borne MMS Payloads. Sensors 15, 6560–6585. doi:10.3390/s150306560.

DJI, 2017. Spreading Wings S1000+ [WWW Document]. URL http://www.dji.com/spreading-wings-s1000-plus (accessed 3.9.17).

Fiorani, F., Schurr, U., 2013. Future scenarios for plant phenotyping. Annu. Rev. Plant Biol. 64, 267–291.

Gerke, M., 2009. Dense matching in high resolution oblique airborne images. Int Arch Photogramm Remote Sens Spat Inf Sci 38, W4.

Habib, A., 2017. Photogrammetric & LiDAR Georeferencing [WWWDocument].URLhttps://engineering.purdue.edu/CE/Aca

demics/Groups/Geomatics/DPRG/Slides_Laser_2017/CH_2 (accessed 3.9.17).

Habib, A., Han, Y., Xiong, W., He, F., Zhang, Z., Crawford, M., 2016. Automated Ortho-Rectification of UAV-Based Hyperspectral Data over an Agricultural Field Using Frame RGB Imagery. Remote Sens. 8, 796.

Habib, A., Xiong, W., He, F., Yang, H.L., Crawford, M., 2017. Improving Orthorectification of UAV-Based Push-Broom Scanner Imagery Using Derived Orthophotos From Frame Cameras. IEEE J. Sel. Top. Appl. Earth Obs. Remote Sens. 10, 262–276.

He, F., Habib, A., 2016. Automated Relative Orientation of UAV-Based Imagery in the Presence of Prior Information for the Flight Trajectory. Photogramm. Eng. Remote Sens. 82, 879–891.

He, F., Habib, A., 2014. Linear approach for initial recovery of the exterior orientation parameters of randomly captured images by low-cost mobile mapping systems. Int. Arch. Photogramm. Remote Sens. Spat. Inf. Sci. 40, 149.

Hirschmuller, H., 2005. Accurate and efficient stereo processing by semi-global matching and mutual information, in: Computer Vision and Pattern Recognition, 2005. CVPR 2005. IEEE Computer Society Conference on. IEEE, pp. 807–814.

Hirschmüller, H., Bucher, T., 2010. Evaluation of digital surface models by semi-global matching.

Honkavaara, E., Saari, H., Kaivosoja, J., Pölönen, I., Hakala, T., Litkey, P., Mäkynen, J., Pesonen, L., 2013. Processing and assessment of spectrometric, stereoscopic imagery collected using a lightweight UAV spectral camera for precision agriculture. Remote Sens. 5, 5006–5039.

Mikhail, E.M., Bethel, J.S., McGlone, J.C., 2001. Introduction to modern photogrammetry. N. Y.

Nistér, D., 2004. An efficient solution to the five-point relative pose problem. IEEE Trans. Pattern Anal. Mach. Intell. 26, 756–770.

Ribera, J., He, F., Chen, Y., Habib, A.F., Delp, E.J., 2016. Estimating Phenotypic Traits From UAV Based RGB Imagery, in: Proceedings of the ACM SIGKDD Conference on Knowledge Discovery and Data Mining, Workshop on Data Science for Food, Energy, and Water. San Francisco.

Velodyne LiDAR, 2017. VLP-16 Users Manual [WWW Document]. URL http://velodynelidar.com/docs/manuals/VLP-16%20User%20Manual%20and%20Programming%20Guide%2063-9243%20Rev%20A.pdf (accessed 3.9.17).

Wallace, L., Lucieer, A., Watson, C.S., 2014. Evaluating tree detection and segmentation routines on very high resolution UAV LiDAR data. IEEE Trans. Geosci. Remote Sens. 52, 7619–7628.

Wallace, L., Lucieer, A., Watson, C., Turner, D., 2012. Development of a UAV-LiDAR system with application to forest inventory. Remote Sens. 4, 1519–1543.

Zhang, C., Kovacs, J.M., 2012. The application of small unmanned aerial systems for precision agriculture: a review. Precis. Agric. 13, 693–712.